PAPER

A study of n-doping in self-catalyzed GaAsSb nanowires using GaTe dopant source and ensemble nanowire near-infrared photodetector

To cite this article: Shisir Devkota et al 2020 Nanotechnology 31 505203

View the article online for updates and enhancements.

Recent citations

- Recent Progress on the Gold-Free Integration of Ternary III—As Antimonide Nanowires Directly on Silicon Ezekiel Anyebe Anyebe
- Epitaxial High-Yield Intrinsic and Te-Doped Dilute Nitride GaAsSbN Nanowire Heterostructure and Ensemble Photodetector Application Rabin Pokharel *et al*



IOP ebooks™

Bringing together innovative digital publishing with leading authors from the global scientific community.

Start exploring the collection-download the first chapter of every title for free.

IOP Publishing Nanotechnology

Nanotechnology 31 (2020) 505203 (10pp)

https://doi.org/10.1088/1361-6528/abb506

A study of n-doping in self-catalyzed GaAsSb nanowires using GaTe dopant source and ensemble nanowire near-infrared photodetector

Shisir Devkota¹, Mehul Parakh¹, Sean Johnson², Priyanka Ramaswamy², Michael Lowe², Aubrey Penn^{3,4}, Lew Reynolds⁴ and Shanthi Iyer¹

- ¹ Nanoengineering, Joint School of Nanoscience and Nanoengineering, North Carolina A&T State University, Greensboro, NC 27401, United States of America
- ² Department of Electrical and Computer Engineering, North Carolina A&T State University, Greensboro, NC 27411, United States of America
- ³ Department of Materials Science and Engineering, North Carolina State University, Raleigh, NC 27695, United States of America
- ⁴ Analytical Instrumentation Facility, North Carolina State University, Raleigh, NC 27695, United States of America

E-mail: iyer@ncat.edu

Received 23 June 2020, revised 25 August 2020 Accepted for publication 3 September 2020 Published 2 October 2020



Abstract

This work reports a comprehensive investigation of the effect of gallium telluride (GaTe) cell temperature variation (T_{GaTe}) on the morphological, optical, and electrical properties of doped-GaAsSb nanowires (NWs) grown by Ga-assisted molecular beam epitaxy (MBE). These studies led to an optimum doping temperature of 550 °C for the growth of tellurium (Te)-doped GaAsSb NWs with the best optoelectronic and structural properties. Te incorporation resulted in a decrease in the aspect ratio of the NWs causing an increase in the Raman longitudinal optical/transverse optical vibrational mode intensity ratio, large photoluminescence emission with an exponential decay tail on the high energy side, promoting tunnel-assisted current conduction in ensemble NWs and significant photocurrent enhancement in the single nanowire. A Schottky barrier photodetector (PD) using Te-doped ensemble NWs with broad spectral range and a longer wavelength cutoff at ~1.2 μ m was demonstrated. These PDs exhibited responsivity in the range of 580–620 A W⁻¹ and detectivity of 1.2–3.8 × 10¹² Jones. The doped GaAsSb NWs have the potential for further improvement, paving the path for high-performance near-infrared (NIR) photodetection applications.

Supplementary material for this article is available online

Keywords: nanowires, molecular beam epitaxy (MBE), Te-doping, near-infrared ensemble photodetector, field emission, low-frequency noise spectroscopy, generation-recombination noise

(Some figures may appear in colour only in the online journal)

1. Introduction

Ensemble nanowires (NWs) in a vertical configuration have been actively investigated as potential building blocks to realize high performance nanostructured optical devices due to their unparalleled ability to concentrate the incident light arising from the pronounced antenna effect [1]. High refractive index mismatch between the NW ensemble and surrounding

air forms the graded refractive index layer leading to its antireflection characteristics [1–3]. Further, the random growth of vertical ensemble NWs with optimum fill factor increases the optical path length due to multiple scattering [4] and suppresses specular absorption. The alignment of incident light propagation to the axis of the NWs [5] also contributes to increased absorption. Cumulative effects of all these results in enhanced efficient coupling of incident light in the NWs compared to thin-film counterparts. In addition, increased density of available electronic states, and reduced density of misfit dislocations in the NWs bode well for photodetection [6, 7], transceivers, photovoltaics [8, 9], biological and chemical sensing applications.

Group III–V NWs, in particular, GaAsSb, have attracted great interest not only because they encompass the important telecommunication wavelength spectral region for low power and high-speed applications [10–12] but also due to ease of bandgap engineering and high structural phase purity, latter stemming from the presence of Sb [13].

The successful performance of optoelectronic devices calls for a well-behaved dopant, namely a low diffusion coefficient and low ionization energy. In the case of NW growth, the choice of dopant becomes even more critical due to the vaporliquid-solid (VLS) mechanism being the dominant growth mechanism, as the incorporated dopant species can modulate droplet formation as well as adatom mobility. Therefore, these have a significant impact on the growth kinetics. In this work, our focus is on the tellurium (Te)-doping of GaAsSb NWs using a gallium telluride (GaTe) captive dopant source. The choice of Te as the dopant amongst the other commonly used n-type dopants, for example, Sn, Si, Se, and S, stems from its high solubility in the Ga droplet associated with the VLS mechanism and a significantly high level of doping that can be achieved at a lower temperature than most of the dopants [14]. Other key advantages of Te-doping include high incorporation efficiency and low diffusion coefficient [15, 16]. Further, the selection of a GaTe captive dopant source in molecular beam epitaxy (MBE) was dictated by its ability to control better the doping level and insignificant cell cross-talk and associated memory issues [17].

There are numerous reports of GaTe source being successfully used as an n-type dopant source in GaAs [18–23] NWs and a report on InAs [24] NWs by Gusken et al. Many of these reports on GaAs NWs (Czaban and Caram) have been focused on n-type doping in the mid- 10^{18} cm⁻³ of ensemble NWs for photovoltaic applications, and the carrier concentration is assumed to be the same as in the thin film configuration. Orru *et al* [21] and Goktas *et al* [23] measured the carrier concentration directly in NWs using different techniques. Effects of GaTe cell temperature (T_{GaTe}) on different properties have been carried out by Soulemenin *et al* [22], and Gusken *et al* [24] The range of T_{GaTe} reported in the literature are quite wide varying from 401 °C–640 °C.

In this work, we present the first results on Te-doping of GaAsSb NWs using a GaTe source. While the GaAs work provides a guideline, those results cannot be directly translated to GaAsSb NWs since the growth temperature for GaAsSb is lower than GaAs, and the presence of two surfactants makes the growth kinetics quite different from GaAs NWs. Hence, we have conducted a systematic and comprehensive investigation on the effects of doping on the structural, optical, vibrational characteristics of ensemble NWs and electrical characteristics of the single nanowire (SNW) by varying the T_{GaTe} . Using the optimized T_{GaTe} of 550 °C and growth conditions that yielded planar defect-free nanowires with the highest photoluminescence (PL) intensity and best photoconduction for a single nanowire, we have successfully demonstrated a Schottky barrier ensemble NW photodetector (PD) in the near-infrared (NIR) region with responsivity in the range of 580–620 A W⁻¹ and detectivity in the order of 10^{12} .

2. Experimental details

Te-doped GaAsSb NWs were grown on chemically cleaned (Piranha/HF) p-Si (111) substrate in a solid source MBE EPI 930 system. At a substrate temperature of 620 °C, the Ga shutter was opened for 13 s before the opening of As shutter for GaAs stem growth. A Te-doped GaAsSb core was subsequently grown by simultaneous opening of Sb and Te shutters at a lower growth temperature of 590 °C for 13 min. After core growth, the substrate temperature was decreased to 465 °C for surface passivation. A droplet residing on the top of the NW associated with the VLS growth mechanism was consumed using the same As flux with the rest of the shutters closed. The NW core was passivated by growing an inner GaAlAs passivation shell for 3 min, followed by a GaAs shell for 2 min to prevent oxidation of Al. During growth, the group III flux was 6×10^{-7} Torr, while the group V flux was 6×10^{-6} Torr, which corresponds to a nominal planar GaAs growth rate of 0.5 ml s⁻¹. As₄ and Sb₂ were the group V constituents used during the growth. A GaTe captive source was used for Te-doping, with temperatures in the range of 500 °C-570 °C for active investigation. The dopant cell was kept idle at the set-point for 1 h to avoid the flux variation due to any temperature fluctuations.

Morphological properties of NWs were assessed using a Carl-Zeiss Auriga-BU FIB field emission scanning electron microscope (FESEM). A Thermo Fisher Talos F200X 80–200 kV scanning/transmission electron microscope (S/TEM) operated at 200 kV was used for imaging, selected area electron diffraction (SAED) patterns, and energy-dispersive x-ray spectroscopy (EDS).

The PL set up consisted of a 633 nm He-Ne laser as the excitation source, a double grating monochromator for wavelength dispersion, liquid nitrogen cooled InGaAs detector and conventional lock-in amplifier techniques for PL emission detection. A closed-cycle optical cryostat, with the sample chamber interfaced with a fiber-coupled confocal microscope, was used to determine the PL characteristics at 4 K. The sample preparation procedure for the SNW PL measurement was reported previously [25]. Room temperature (RT)

Raman spectroscopy was performed in a Horiba Jobin Yvon ARAMIS Raman microscope with a He-Ne laser (633 nm) excitation source.

Conductive atomic force microscopy operating in contact mode was used for room temperature I-V characteristics of single NWs. Platinum (Pt) coated silicon (Si) cantilever having a radius of 20 nm with a spring constant of 18 N m⁻¹ was used as the probe. The I-V characteristics for Te-doped NWs were carried out by placing the atomic force microscope (AFM) probe to the NW tip, and back contact was made to the substrate for a voltage sweep from -1.4 V to +1.4 V. An IR laser of 860 nm wavelength was used as an excitation source for photosensitivity assessment. An ensemble PD device was fabricated by spin-coating polymethyl methacrylate (PMMA) as the filling layer in the ensemble NWs with tips exposed by oxygen plasma etcher for top contact. Details on the fabrication of ensemble PD can be found elsewhere [26]. The electrical properties of the ensemble PD device were assessed using a two-probe technique. The response of the PD to illumination was determined using Keithly source meter interfaced with the microHR spectrometer with the tungstenhalogen lamp as the excitation source. Low-frequency noise spectroscopy set up is based on a cross-correlation technique, consisting of two independent low noise current preamplifiers connected to the device, while its outputs are connected to two different channels of the digital signal analyzer (DSA). The frequency-dependent noise measurement was taken at a reverse bias of 1 V, and data represent an average of 100 spectral runs.

3. Results and discussion

First, for reference, Te-doped GaAs NWs were grown with T_{GaTe} varying over a wide range from 200 °C to 570 °C. Low temperature (4 K) PL spectra of Te-doped GaAs NWs remained essentially invariant relative to intrinsic NWs up to 400 °C and showed significant enhancement in intensity beyond 500 °C with 550 °C being the optimum cell temperature exhibiting the highest intensity. These are shown in supporting information figure S1 (available online at https://stacks.iop.org/NANO/31/505203/mmedia). Hence, a study on the Te-doping of GaAsSb NWs was confined over a narrow T_{GaTe} window of 500 °C–570 °C.

3.1 Structural and optical characteristics

SEM images of intrinsic, NWs doped at T_{GaTe} of 550 °C and 570 °C referred to as sample R, 550, and 570 hereafter (figures 1(a–c)) reveal high-density vertical NWs. A mean length and diameter of the sample R were \sim 2.4 \pm 0.12 μ m and 136 \pm 6 nm, respectively. However, in comparison to sample R, the average length of both samples 550 and 570 shrunk to \sim 1.7 \pm 0.08 μ m and 1.75 \pm 0.1 μ m, respectively, with a corresponding increase in the average diameter of \sim 152 \pm 7 nm and 157 \pm 5 nm. The lowering of the NW aspect ratio of doped NWs (figure 1(d)) is a signature of the surfactant nature of Te. This is attributed to Te atoms occupying As lattice sites

[27] forming a strong bond with the NWs crystal lattice, which impede adatom migration while shrinking the adatom surface diffusion length (SDL) [28]. The NWs exhibited high uniformity in diameter along the length, as shown in supporting information figure S2, though there is a variation in the diameter amongst the NWs.

Next, the effect of Te-doping on the optical properties of the doped NWs in comparison to intrinsic ones was assessed at 4 K and RT via PL spectroscopy. The variation of the 4 K PL peak energy and its intensity as a function of T_{GaTe} (figure 2(a)) demonstrated a gradual redshift (a maximum of 90 meV) accompanied by significant intensity enhancement. Also, the RT PL spectral shape transforms from symmetric for intrinsic NWs to an asymmetric shape in the doped NWs that exhibits a high energy PL tail (figure 2(b)) with sharper low energy onset. The lack of sharp low energy onset in the intrinsic seems to suggest the presence of a low energy shoulder, potentially due to defects, attributed to acceptor vacancies [29], which are filled up by doping and therefore vanishes for the doped samples. The long exponential decay tail is associated with radiative recombination occurring from Te-bound impurity localized states [30]. Amongst the R and doped NWs, sample 550 displayed the best PL characteristics with the highest PL emission intensity at 4 K (figure 2(c)) accompanied by low full-width half-maximum at both RT and 4 K, suggesting T_{GaTe} of 550 °C to be the optimum doping temperature with superior optical properties.

Figure 2(d) illustrates a comparison of the RT Raman spectra for samples R, 550, and 570. All the samples exhibited distinct GaAs-like transverse optical (TO) and longitudinal optical (LO) vibrational modes. The TO and LO modes of samples 550 were redshifted relative to intrinsic NWs, speculated due to dampening of the lattice vibration frequency by incorporation of the heavier Te atoms. Furthermore, an increased LO/TO signal ratio in 550 sample very likely originated from the combined effect of increased density of ionized species leading to higher electric field coupling and increased NW diameter, which manifests in the enhanced LO mode [31]. An additional peak positioned at \sim 232 cm⁻¹ is assigned to the GaSb-like TO mode, which is commonly observed for higher Sb concentration in the GaAs matrix [25, 32]. All the above changes in the 550 sample relative to intrinsic ones, namely, the decrease in aspect ratio, enhanced PL emission accompanied by the asymmetric line shape with the high energy band tail and increased LO/TO mode ratio in the Raman spectra of the doped NWs support Te incorporation in the host lattice. However, the Raman spectra of 570 sample shifts closer to the intrinsic sample with a broader linewidth and asymmetric line shape of LO peak. This reversal in the peak shifts and LO/TO signal ratio with increased GaTe cell temperature are speculated to be caused by Te-induced defects, which is also corroborated by increased planar defects on the tip of the NWs, as evidenced from the high-resolution transmission electron microscope (HRTEM) images in the supporting information figure S3. It is to be noted that the repeated growths ensured that this reversal of the characteristics at higher T_{GaTe} of 570 °C is reproducible and is not a result of the artifact of source depletion or any growth sequence.

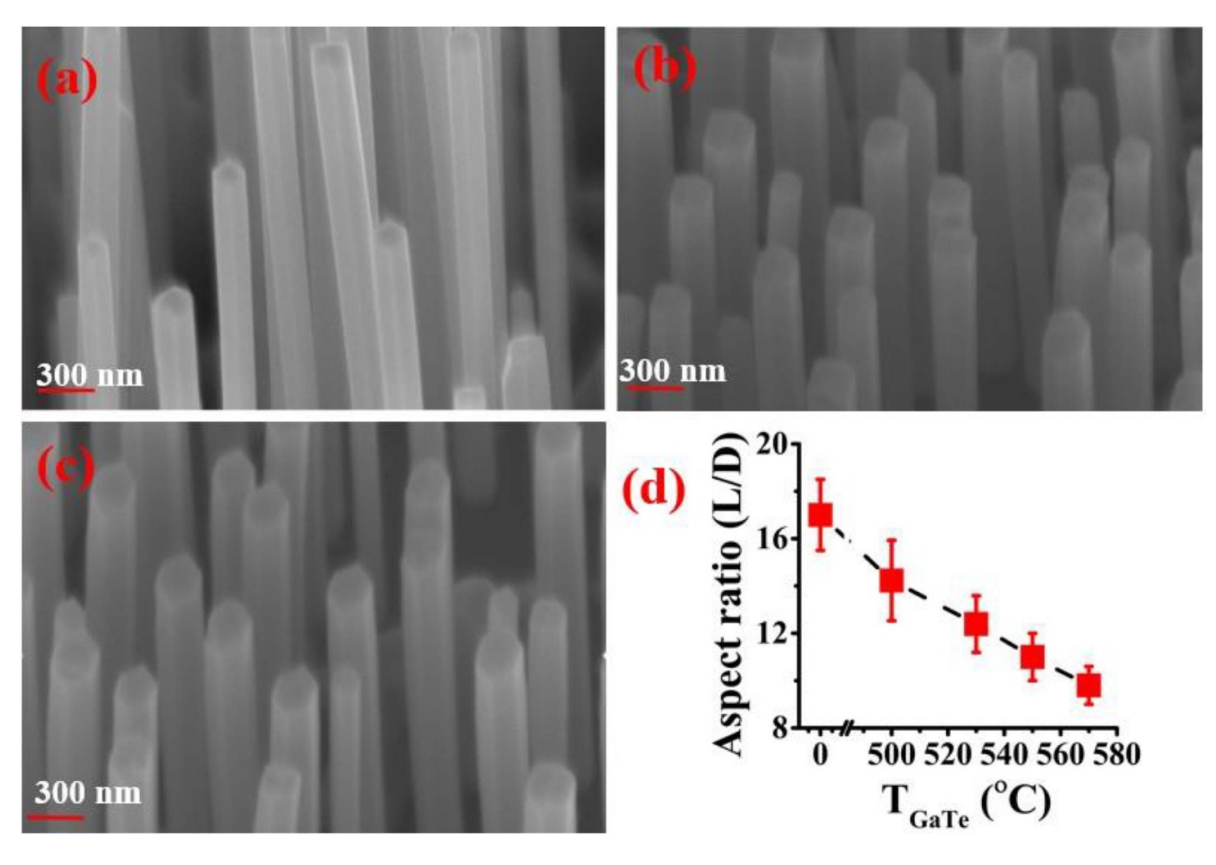


Figure 1. High magnification SEM images of GaAsSb NWs: (a) intrinsic, (b) 550, (c) 570 samples, and (d) variation of the aspect ratio of the NWs with $T_{\text{GaTe.}}$

3.2 Electrical characteristics of SNW

The I-V characteristics of the intrinsic and doped vertical SNW for varying T_{GaTe} were investigated using C-AFM. The schematic of SNW I-V measurements using AFM is depicted in figure 3(a). Doped NWs were characterized by a lower turnon voltage (figure 3(b)) due to the doping-induced reduction in the depletion region width. Amongst all the doped samples, 550 showed superior photoconductivity, as evidenced by the higher photocurrent to the dark current ratio (I_P/I_D) at a reverse bias of -1 V (figure 3(c)). The exponential dependence of the dark current under reverse bias in 550 (figure 3(d)) with a concomitant reduction in the turn-on voltage is indicative of the tunneling assisted conduction being the dominant transport mechanism. The sample 550 demonstrated a responsivity and a detectivity of $0.3~A~W^{-1}$ and 4.8×10^8 Jones, respectively. The values are much lower than the responsivity of 1463 A W⁻¹ at 532 nm and detectivity of 6.6×10^9 Jones reported by Huh et al [33] and the responsivity of 325.1 A W^{-1} at 1.3 μ m and the detectivity of 4.7 \times 10¹⁰ Jones reported by Li et al [34] on horizontal GaAsSb SNW. An effective optical absorption throughout the NW in the horizontal configuration very likely contributes to the enhanced device responsivity reported.

4 K PL spectra carried on SNW of 550 (supporting information figure S4) were similar to that for corresponding ensemble NWs, indicating good compositional homogeneity amongst the NWs. As these optical and electrical observations indicate

that sample 550 has the optimized doping level with good PL emission and photoconduction, the following structural analysis using TEM as well as PD fabrication on ensemble NWs was confined to sample 550 only.

3.3 Microstructural characteristics

Figure 4(a) shows the TEM image of a 550 NW grown under the optimized condition. The HRTEM image (figures 4(b–d)) and SAED pattern (figures 4(e–g)) confirm the single-phase zinc-blende (ZB) crystal structure of n-GaAsSb NWs. The bottom and middle segments of the NWs were free of any planar defects, while the top segment revealed stacking faults of ~20 nm distinctly seen as horizontal contrast stripes (figure 4(b)). The occurrence of these structural defects near the NW tip is very likely due to the procedure adopted for the Ga droplet consumption, which was carried out under As ambient. The increased concentration of As favors the wurtzite (WZ) crystal phase, and it is well established that stacking faults originate due to transformation from ZB to WZ phase [35].

The EDS compositional line scans (figures 4(i–k)) performed at the top, middle, and bottom segments are depicted in the high angle annular dark-field (HAADF) STEM image in figure 4(h). The presence of extended plateau of all the constitutional elements in the EDS line scan at the bottom and middle segments suggests radial compositional

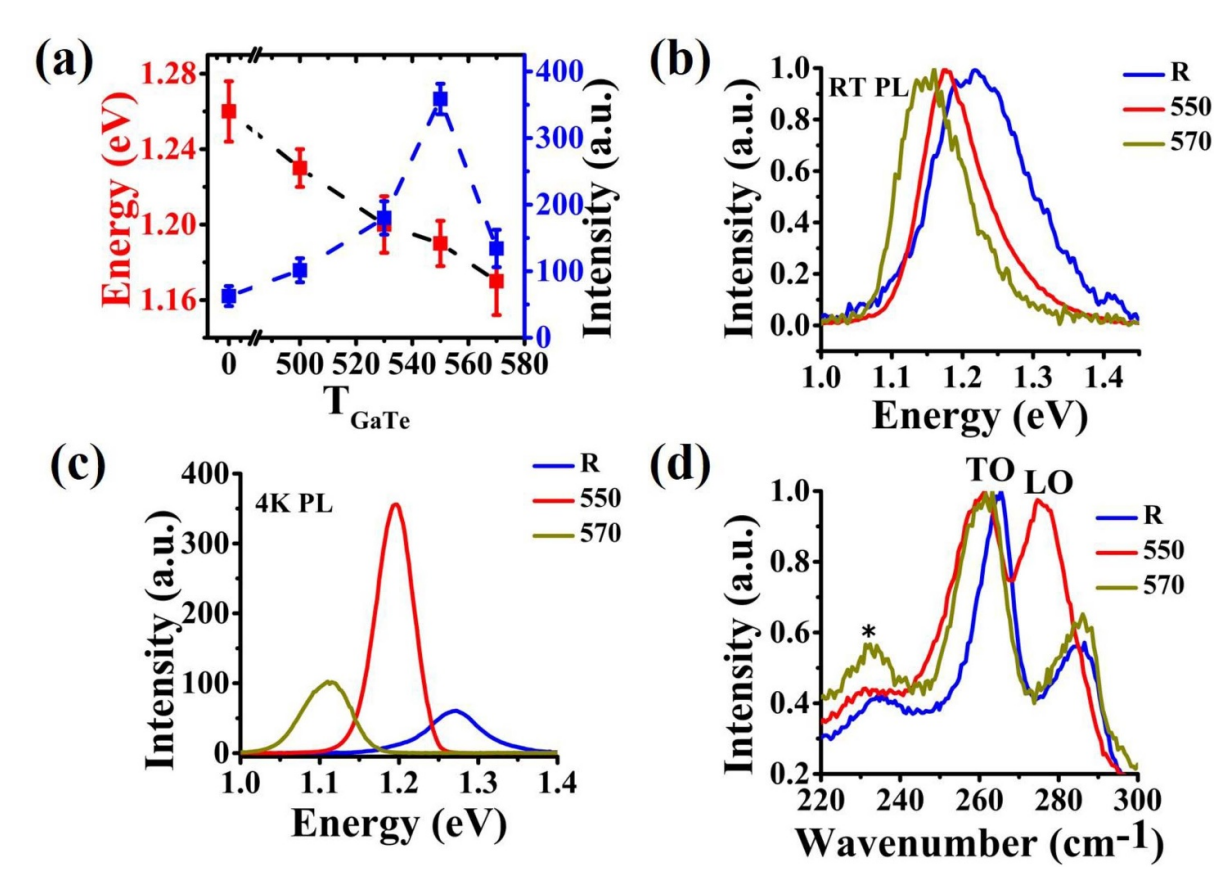


Figure 2. (a) Variation of 4 K PL peak energy (red spheres) and its intensity (blue spheres) with T_{GaTe} (dotted black and blue lines are guides for the eye), superimposed (b) normalized RT PL, (c) 4 K PL, and (d) RT Raman spectra of samples R, 550 and 570. The asterisk at \sim 232 cm⁻¹ represents the GaSb-like TO mode.

homogeneity. However, the top segment of the NW shows radial compositional inhomogeneity, which is again attributed to the termination of the Ga droplet. EDS line scan at the middle and bottom segments of the NW reveal an Sb deficiency at the surface resulting from the As-Sb exchange mechanism due to the extended exposure of NWs to the group V fluxes causing out diffusion of Sb [33].

It is to be pointed out that HRTEM of 570 samples revealed similar planar defect-free structure in the bottom and middle segments (not shown) while showing a higher density of stacking faults at the top (supporting information figure S3), indicating the doping induced disorder for higher T_{GaTe} . This explains the observed degradation in the PL intensity and the photocurrent in 570 samples and also demonstrates that a high density of stacking faults at the NW tip can have a deleterious impact on the optoelectronic characteristics of the NWs.

3.4 Ensemble NW photodetector

The performance of ensemble PD (supporting information figure S5) fabricated using sample 550 was assessed using RT I–V characteristics under dark and illumination conditions. First, the dark I–V was examined for the prevalent current transport mechanism. An ideality factor of 8.8 and series resistance of $\sim\!320~\text{k}\Omega$ were extracted from the slope and intercept, respectively from the plot of differential change in the

voltage (dV) to differential change in current (dI) versus reciprocal of current (1/I) under forward bias above the turn-on voltage (not shown here). The large series resistance is attributed to the contact resistance as no special process such as annealing after metal deposition was performed. The higher ideality factor corroborates our earlier discussion on tunneling being the dominant current conduction mechanism in a single NW. Alternatively, we can model the I–V data based on a non-ideal Schottky diode equation to estimate the carrier concentration by best fit to the experimental dark I–V curve using a generalized expression for an exponential fit in forward bias (figure 5(a) inset), as shown below.

$$I = Aexp(B \times V) \tag{1}$$

Here, A is the reverse saturation current. B is used to determine the Padovani-Stratton parameter (E_{00}) , also known as the tunneling parameter employing the following equations [36]:

$$B = \frac{1}{E_{00} \coth\left(\frac{E_{00}}{KT}\right)}$$
 (2)

$$E00 = \frac{qh}{4\pi} \sqrt{\frac{N_d}{m^* \varepsilon}} \tag{3}$$

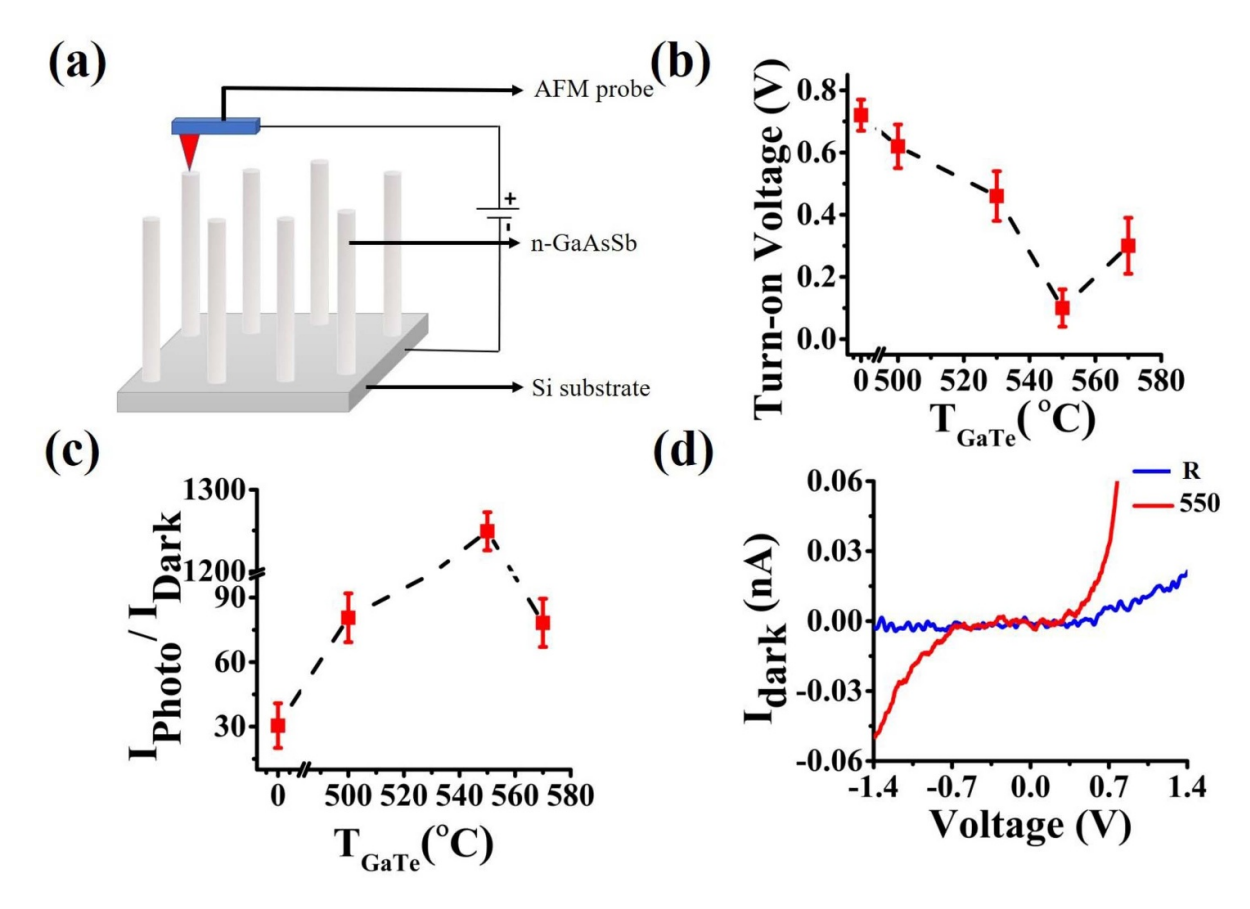


Figure 3. (a) Schematic of SNW C-AFM I–V measurement, variation of (b) photocurrent turn-on voltage, (c) photocurrent to the dark current ratio (I_P/I_D) with T_{GaTe} , and (d) superimposed dark current of the samples R and 550.

Here m^* represents the electron effective mass, q the electronic charge, h the Planck's constant and ε the semiconductor permittivity. The best fit for the experimental data resulted in an E_{00} of ~ 0.3 eV from which a carrier concentration of 4×10^{19} cm⁻³ was extracted. The high carrier concentration estimated from simulation fits very well with the value of 3.3 \times 10¹⁹ cm⁻³ and 2.3 \times 10¹⁹ cm⁻³ determined from other surface analytical techniques x-ray photoelectron spectroscopy (XPS) and ultra violet photoelectron spectroscopy (UPS), respectively [37]. Further, the value of carrier concentration also in excellent agreement with those reported earlier by Bennet et al [38]. on GaAs and GaSb thin films at this GaTe cell temperature. A good agreement between the simulated data and the value obtained from surface analytical techniques, suggest that Te is not amphoteric as Si as suggested by Dubrovskii et al [39] and also the incorporation predominantly occurs through the droplet via the VLS mechanism. The absence of Te-related distinct vibrational modes in Raman spectra corroborate the carrier concentration to be less than 10²⁰ cm⁻³ in our doped NWs and Te not being incorporated in Ga lattice sites [40, 41]. The value of E_{00} > kT indicates current transport by field emission (FE) [42] being the dominant mechanism. Operating under RT conditions, excellent photosensitivity was revealed by a significant I_P/I_D of $\sim 1.3 \times 10^5$ at $\sim 1.07 \ \mu m$ illumination corresponding to the bandgap of GaAsSb (\sim 8% Sb) at a reverse applied bias of -1 V (figure 5(a)). The PD spectral response was broad, covering the visible region with a longer wavelength cutoff at \sim 1.2 μ m (figure 5(b)). The estimated responsivity is \sim 620 A W⁻¹ with an external quantum efficiency (EQE) of 7×10^4 %. At higher wavelengths, the roll-off of the photocurrent occurs slightly above the bandgap of GaAsSb when the energy of incoming photons becomes less than the bandgap and is not absorbed. The reduction in the photocurrent on the lower wavelength side of \sim 0.5 μ m is dictated by a combination of thermalization of hot carriers, screening of the electric field by the photogenerated carriers, and enhanced surface absorption [43].

Excitation power dependence of the photocurrent at different bias voltage is depicted in figure 5(c). The photocurrent shows a slight dip above certain excitation power, being more pronounced with step-like behavior at lower bias. We attribute this response to the trap filling effects [44]. The lower voltages enable probing of shallow traps while at higher biases carriers are detrapped from shallow traps due to the large electric field.

Low-frequency noise (LFN) spectroscopy (figure 5(d)) exhibited a noise power spectral density (PSD) roll-off after 4 Hz. The best Lorentzian fit of the roll-off data up to 20 Hz (figure 5(d) inset) suggests generation-recombination noise as the principal contributor. Beyond

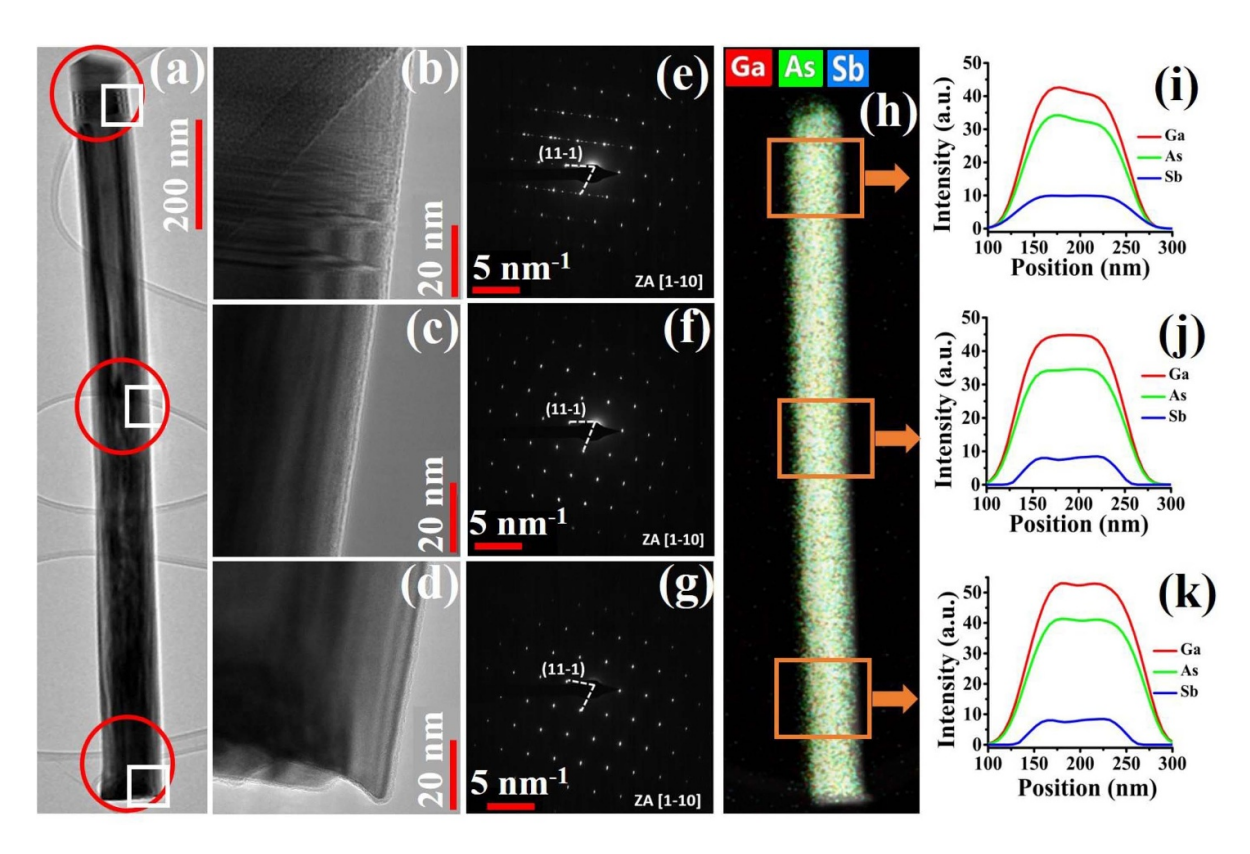


Figure 4. Optimized n-GaAsSb NW: (a) TEM image, (b–d) HRTEM images of the selected areas marked with the white squares, (e-g) SAED patterns of the selected regions of NW in figure (a) marked with red circles viewed from the zone axis of [1–10], (h) False color mapping of HAADF STEM image of the corresponding NW, and (i–k) EDS line scans taken at the top, middle, and bottom segments marked with orange rectangles in figure (h).

20 Hz, frequency-independent noise is observed. Based on the PL spectral shape and power dependence of photocurrent, we attribute the presence of generation-recombination noise to a shallow trap arising from band tail states. Under reverse biased conditions, traps act as generation-recombination centers affecting the device performance and adding to overall device noise [45].

Photodetectors with responsivity variations $580-620 \text{ A W}^{-1}$, noise equivalent power (NEP) in the range of $2.3-4.7 \times 10^{-13}$ W, and associated detectivity of 1.2- 3.8×10^{12} Jones were obtained in the spectral range of $0.63~\mu m$ to $1.1~\mu m$. In the literature, there has been limited work on the fabrication of ensemble NW PDs. In the AlGaAs/GaAs [46] ensemble NW configuration, the responsivity was reported to be ~ 0.7 A W⁻¹ at 850 nm. In InGaAs [47] nanopillars ensemble PDs, the peak responsivity of 0.28 A W^{-1} at 1100 nm was obtained. In both these devices, the detectivity of the PDs was not reported. In our earlier work, we have reported a responsivity of 311 A W⁻¹ and detectivity of 1.9×10^{10} Jones at 633 nm for p-i GaAsSb [48] NWs. Our device metrics in this report, namely responsivity, and detectivity are significantly higher than those reported in ensemble NW configuration thus far. There is significant room for improvement in the device performance by using high transmittance transparent contacts and contact annealing, as well as use of arrayed NW configuration that would significantly enhance uniformity amongst the NWs.

4 Conclusion

Te-doping using a GaTe captive source has been successfully demonstrated to be a good dopant for n-type doping in GaAsSb NWs, as evidenced by enhanced PL emission, and the increased photocurrent with the significant reduction in turn-on voltage. Replication of PL and I-V characteristics in an SNW, in ensemble NWs as well S/TEM studies attest to the compositional homogeneity in the NWs. Tebound shallow tail states are found to be responsible for an asymmetric PL line shape with a tail extending on the high energy side and correlate well with a field emission tunneling transport electrical conduction mechanism and lowfrequency generation-recombination noise. The ensemble PD fabricated exploiting the optimized n-GaAsSb NW characteristics demonstrated a broad spectral response with long cut off wavelength of 1.2 μ m and improved responsivity of 580– 620 A W $^{-1}$ with detectivity in the range of 1.2 \times 10 12 - 3.8×10^{12} Jones, compared to the reports in the literature in this and other material systems in this NIR wavelength region.

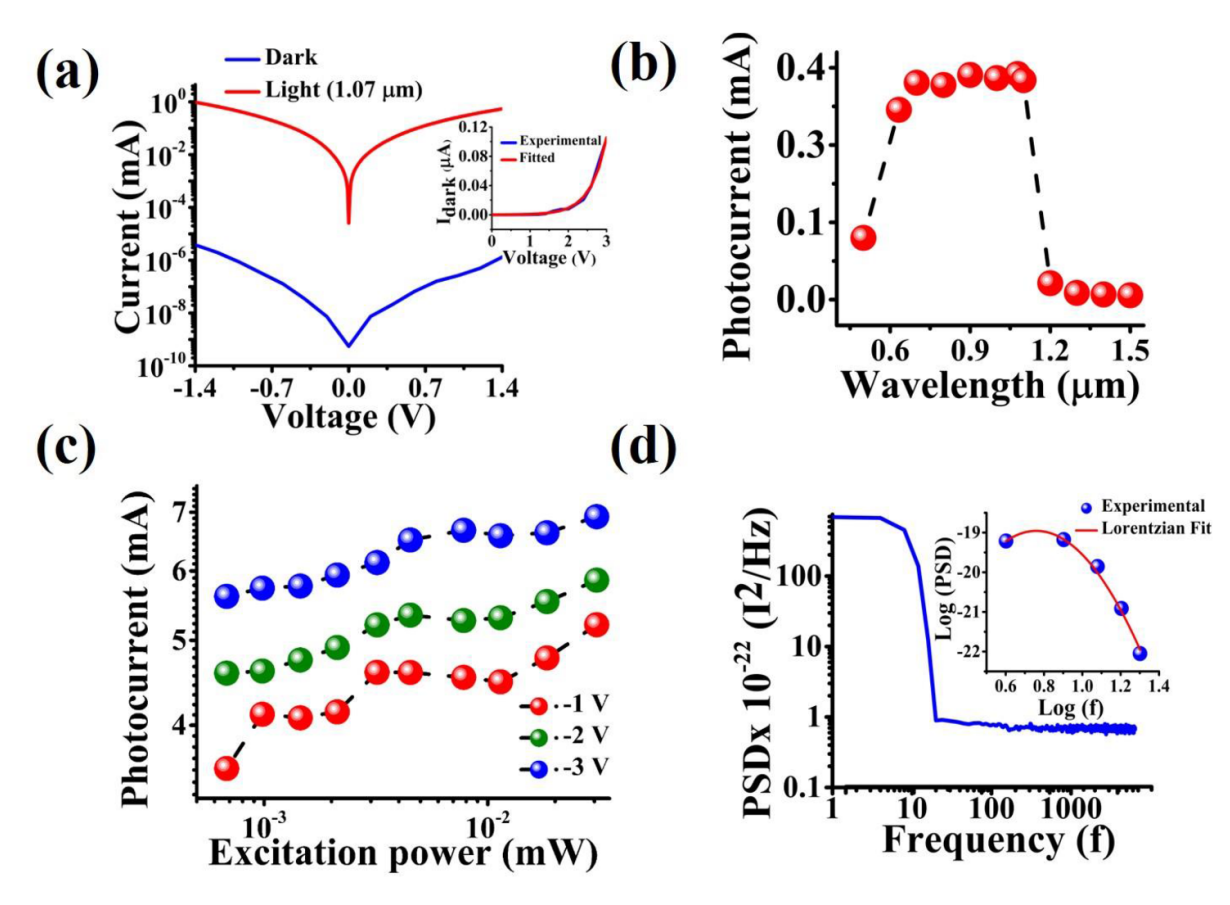


Figure 5. N-GaAsSb NW ensemble PD device: (a) dark and photocurrent (at \sim 1.07 μ m) superimposed in semi-log scale and the inset shows the Schottky diode fitting to calculate tunneling parameter (E₀₀), (b) spectral response, (c) excitation power dependent photocurrent at -1 V, -2 V and -3 V bias for 0.63 μ m laser excitation, (d) dark current noise spectra (S_I) at the reverse applied bias of 1 V, and the inset shows the Lorentzian fit of dark current noise after the roll-off.

Prospects for further improvement in the device performance is very promising with better transparent contact and annealing as well as fabricating the device using patterned nanowire configuration.

Acknowledgments

This work is primarily based upon research supported by the Air Force Office of Scientific Research (AFOSR) under Grant No. W911NF1910002. A part of this work was also supported by the National Science Foundation under Grant No. ECCS-1832117. This work was performed at the Joint School of Nanoscience and Nanoengineering, a member of the Southeastern Nanotechnology Infrastructure Corridor (SENIC) and National Nanotechnology Coordinated Infrastructure (NNCI), which is supported by the National Science Foundation (Grant No. ECCS-1542174). This work was performed in part at the Analytical Instrumentation Facility (AIF) at North Carolina State University, which is supported by the State of North Carolina and the National Science Foundation (Grant No. ECCS-1542015). The AIF is a member of the North Carolina Research Triangle Nanotechnology Network (RTNN), a site in the National Nanotechnology Coordinated Infrastructure (NNCI).

ORCID iDs

Mehul Parakh https://orcid.org/0000-0003-0014-7443 Shanthi Iyer https://orcid.org/0000-0002-8163-9943

References

- [1] Diedenhofen S L, Vecchi G, Algra R E, Hartsuiker A, Muskens O L, Immink G, Bakkers E P, Vos W L and and Rivas J G J A M 2009 Broad-band and omnidirectional antireflection coatings based on semiconductor nanorods Adv. Mater. 21 973–8
- [2] Lee Y-J, Ruby D S, Peters D W, McKenzie B B and and Hsu J W J N L 2008 ZnO nanostructures as efficient antireflection layers in solar cells *Nano Lett.* 8 1501–5
- [3] Chattopadhyay S, Huang Y, Jen Y-J, Ganguly A, Chen K and Chen L J M S 2010 Anti-reflecting and photonic nanostructures *Reports E. R.* 69 1–35
- [4] Muskens O L, Rivas J G, Algra R E, Bakkers E P and Lagendijk A 2008 Design of light scattering in nanowire materials for photovoltaic applications *Nano Lett*. 8 2638–42
- [5] Wang B and Leu P W J O L 2012 Tunable and selective resonant absorption in vertical nanowires *Optics Lett.* 37 3756–8
- [6] Zhang A, You S, Soci C, Liu Y, Wang D and Lo Y-H J A P L 2008 Silicon nanowire detectors showing phototransistive gain Appl. Phys. Lett. 93 121110

- [7] Ahn Y, Dunning J and Park J J N L 2005 Scanning photocurrent imaging and electronic band studies in silicon nanowire field effect transistors *Nano Lett.* 5 1367–70
- [8] Garnett E and Yang P J N L 2010 Light trapping in silicon nanowire solar cells *Nano Lett.* 10 1082–7
- [9] Jung J-Y, Zhou K, Um H-D, Guo Z, Jee S-W, Park K-T and Lee J-H J O L 2011 Effective method to extract optical bandgaps in Si nanowire arrays *Optics Lett.* 36 2677–9
- [10] Alarcón-Lladó E, Conesa-Boj S, Wallart X, Caroff P and I Morral A F 2013 Raman spectroscopy of self-catalyzed GaAs1 – xSbx nanowires grown on silicon *Nanotechnology* 24 405707
- [11] Conesa-Boj S N, Kriegner D, Han X-L, Plissard S B, Wallart X, Stangl J, Fontcuberta I Morral A and Caroff P 2013 Gold-free ternary III–V antimonide nanowire arrays on silicon: twin-free down to the first bilayer *Nano Lett*. 14 326–32
- [12] Li Z, Yuan X, Fu L, Peng K, Wang F, Fu X, Caroff P, White T P, Tan H H and Jagadish C 2015 Room temperature GaAsSb single nanowire infrared photodetectors *Nanotechnology* 26 445202
- [13] Li L, Pan D, Xue Y, Wang X, Lin M, Su D, Zhang Q, Yu X, So H and Wei D 2017 Near full-composition-range high-quality GaAs1–x Sb x nanowires grown by molecular-beam epitaxy *Nano Lett.* **17** 622–30
- [14] Jin Y 2010 Influence of N Incorporation on the Electronic Properties of Dilute Nitride (IN) GaAsN Alloys
- [15] Houng Y-M and Low T 1986 Te doping of GaAs and AlxGa1 – xAs using diethyltellurium in low pressure OMVPE J. Cryst. Growth 77 272–80
- [16] Sun S, Armour E, Zheng K and Schaus C 1991 zinc and tellurium doping in gaas and alxga1 – xas grown by mocvd J. Cryst. Growth 113 103–12
- [17] Bennett B R, Magno R and Papanicolaou N 2003 Controlled n-type doping of antimonides and arsenides using GaTe J. Cryst. Growth 251 532–7
- [18] Caram J, Sandoval C, Tirado M, Comedi D, Czaban J, Thompson D and LaPierre R 2010 Electrical characteristics of core–shell p–n GaAs nanowire structures with Te as the n-dopant *Nanotechnology* 21 134007
- [19] Czaban J A, Thompson D A and LaPierre R R 2009 GaAs core—shell nanowires for photovoltaic applications *Nano Lett.* 9 148–54
- [20] Hakkarainen T, Piton M R, Fiordaliso E M, Leshchenko E D, Koelling S, Bettini J, Galeti H V A, Koivusalo E, Gobato Y G and de Giovanni Rodrigues A 2019 Te incorporation and activation as n-type dopant in self-catalyzed GaAs nanowires *Phys. Rev. Mater.* 3 086001
- [21] Orrù M, Repiso E, Carapezzi S, Henning A, Roddaro S, Franciosi A, Rosenwaks Y, Cavallini A, Martelli F and Rubini S A 2016 Roadmap for controlled and efficient n-type doping of self-assisted GaAs nanowires grown by molecular beam epitaxy Adv. Funct. Mater. 26 2836–45
- [22] Suomalainen S, Hakkarainen T, Salminen T, Koskinen R, Honkanen M, Luna E and Guina M 2015 Te-doping of self-catalyzed GaAs nanowires Appl. Phys. Lett. 107 012101
- [23] Goktas N I, Fiordaliso E M and LaPierre R 2018 Doping assessment in GaAs nanowires *Nanotechnology* 29 234001
- [24] Güsken N A, Rieger T, Mussler G, Lepsa M I and Grützmacher D 2019 Influence of Te-doping on catalyst-free VS InAs nanowires *Nanoscale Res. Lett.* 14 179
- [25] Nalamati S, Sharma M, Deshmukh P, Kronz J, Lavelle R, Snyder D, Reynolds C L, Liu Y and Iyer S A 2019 Study

- of GaAs1-xSbx axial nanowires grown on monolayer graphene by Ga-assisted molecular beam epitaxy for flexible near infrared photodetectors *ACS Appl. Nano Mater.* **2** 4528–37
- [26] Parakh M, Johnson S, Pokharel R, Ramaswamy P, Nalamati S, Li J and Iyer S 2019 Space charge limited conduction mechanism in GaAsSb nanowires and the effect of in situ annealing in ultra-high vacuum *Nanotechnology* 31 025205
- [27] Hurle D 1999 A comprehensive thermodynamic analysis of native point defect and dopant solubilities in gallium arsenide J. Appl. Phys. 85 6957–7022
- [28] Massies J and Grandjean N J P R B 1993 Surfactant effect on the surface diffusion length in epitaxial growth *Phys. Rev. B* 48 8502
- [29] Hakala M, Puska M J and Nieminen R M 2002 Native defects and self-diffusion in GaSb J. Appl. Phys. 91 4988–94
- [30] Iyer S, Hegde S, Abul-Fadl A, Bajaj K and Mitchel W 1993 Growth and photoluminescence of GaSb and Ga 1-x In x As y Sb 1-y grown on GaSb substrates by liquid-phase electroepitaxy *Phys. Rev.* B 47 1329
- [31] Shiang J, Wolters R and Heath J 1997 Theory of size-dependent resonance Raman intensities in InP nanocrystals *J. Chem. Phys.* **106** 8981–94
- [32] Ahmad E, Karim M R, Hafiz S B, Reynolds C L, Liu Y and Iyer S 2017 A two-step growth pathway for high Sb incorporation in GaAsSb nanowires in the telecommunication wavelength range *Sci. Rep.* **7** 10111
- [33] Huh J, Yun H, Kim D-C, Munshi A M, Dheeraj D L, Kauko H, van Helvoort A T, Lee S, Fimland B-O and Weman H 2015 Rectifying single GaAsSb nanowire devices based on self-induced compositional gradients *Nano Lett*. 15 3709–15
- [34] Li Z, Yuan X, Gao Q, Yang I, Li L, Caroff P, Allen M, Allen J, Tan H H and Jagadish C 2020 In situ passivation of GaAsSb nanowires for enhanced infrared photoresponse *Nanotechnology* 31 244002
- [35] Boulanger J, Chia A, Wood B, Yazdi S, Kasama T, Aagesen M and LaPierre R 2016 Characterization of a Ga-assisted GaAs nanowire array solar cell on Si substrate *IEEE J. Photovolt.* 6 661–7
- [36] Padovani F and Stratton R 1966 Field and thermionic-field emission in Schottky barriers *Solid State Electron*. 9 695–707
- [37] Ramaswamy P et al 2020 A study of dopant incorporation in Te-doped GaAsSb nanowires using a combination of XPS/UPS, and C-AFM/SKPM Private Communication
- [38] Bennett B, Magno R, Ikossi K, Papanicolaou N, Boos J and Shanabrook B 2002 In Controlled n-type doping of antimonide/arsenide heterostructures using GaTe Int. Conf. on Molecular Bean Epitaxy (IEEE) pp 183–4
- [39] Dubrovskii V, Hijazi H, Isik Goktas N and LaPierre R R 2020 Be, Te and Si doping of GaAs nanowires: theory and experiment *J. Phys. Chem.* C **124** 17299–307
- [40] Hilse M, Ramsteiner M, Breuer S, Geelhaar L and Riechert H 2010 Incorporation of the dopants Si and Be into GaAs nanowires Appl. Phys. Lett. 96 193104
- [41] Fukata N, Sato K, Mitome M, Bando Y, Sekiguchi T, Kirkham M, Hong J-I, Wang Z L and Snyder R L 2010 Doping and Raman characterization of boron and phosphorus atoms in germanium nanowires ACS Nano 4 3807–16
- [42] Sze S M and Ng K K 2006 *Physics of Semiconductor Devices* (New York: Wiley)
- [43] Yu W J, Liu Y, Zhou H, Yin A, Li Z, Huang Y and Duan X 2013 Highly efficient gate-tunable photocurrent generation in vertical heterostructures of layered materials *Nat. Nanotechnol.* 8 952

- [44] Soci C, Zhang A, Xiang B, Dayeh S A, Aplin D, Park J, Bao X, Lo Y-H and Wang D 2007 ZnO nanowire UV photodetectors with high internal gain *Nano Lett.* **7** 1003–9
- [45] Shockley W and Read W Jr 1952 Statistics of the recombinations of holes and electrons *Phys. Rev.* **87** 835
- [46] Seyedi M A, Yao M, O'Brien J, Wang S and and Dapkus P D J A P L 2013 Large area, low capacitance, GaAs nanowire photodetector with a transparent Schottky collecting junction Appl. Phys. Lett. 103 251109
- [47] Senanayake P, Hung C-H, Shapiro J, Lin A, Liang B, Williams B S and Huffaker D 2011 Surface plasmon-enhanced nanopillar photodetectors *Nano Lett.* 11 5279–83
- [48] Sharma M, Ahmad E, Dev D, Li J, Reynolds C L Jr, Liu Y and Iyer S J N 2018 Improved performance of GaAsSb/AlGaAs nanowire ensemble Schottky barrier based photodetector via in situ annealing *Nanotechnology* 30 034005

1 A study of n-doping in self-catalyzed GaAsSb nanowires using GaTe

2 dopant source and ensemble nanowire near-infrared photodetector

- 3 Shisir Devkota¹, Mehul Parakh¹, Sean Johnson², Priyanka Ramaswamy², Michael Lowe², Aubrey
- 4 Penn^{3,4}, Lew Reynolds^{4,} and Shanthi Iyer¹

5

12

13

14

15 16

17

18

6 Nanoengineering, Joint School of Nanoscience and Nanoengineering, North Carolina A&T State

- 7 University, Greensboro, North Carolina 27401, USA
- 8 ² Department of Electrical and Computer Engineering, North Carolina A&T State University,
- 9 Greensboro, North Carolina 27411, USA
- ³ Department of Materials Science and Engineering, North Carolina State University, Raleigh, NC 27695
- ⁴ Analytical Instrumentation Facility, North Carolina State University, Raleigh, NC 27695, USA.

Section 1: Variation of PL intensity of doped GaAs NWs at different T_{GaTe}

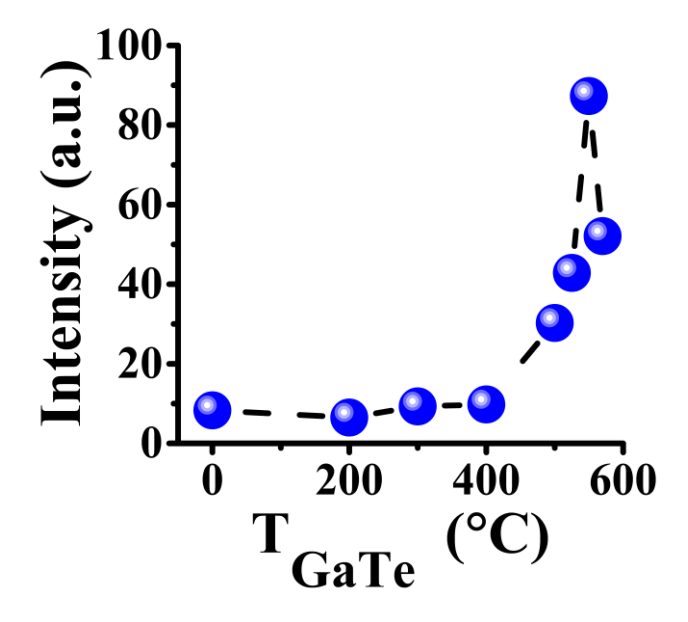


Figure S1. Variation of 4K PL intensity in Te doped GaAs NWs at different T GaTe

- 19 For the optimization of T_{GaTe}, GaAs NWs were doped to the GaTe cell temperature of 200-570 °C.
- 20 Both the intrinsic and doped NWs were characterized optically using photoluminescence (4K PL).
- 21 As depicted in figure S1, PL intensity was improved significantly for the NWs doped at T_{GaTe}
- 22 above 500 °C, indicative of significant doping of the NWs beyond 500 °C. Thus, the narrow T_{GaTe}
- window of 500-570 °C was utilized in the doping study of GaAsSb NWs.

Section S2: Structural properties of the Te-doped SNW:

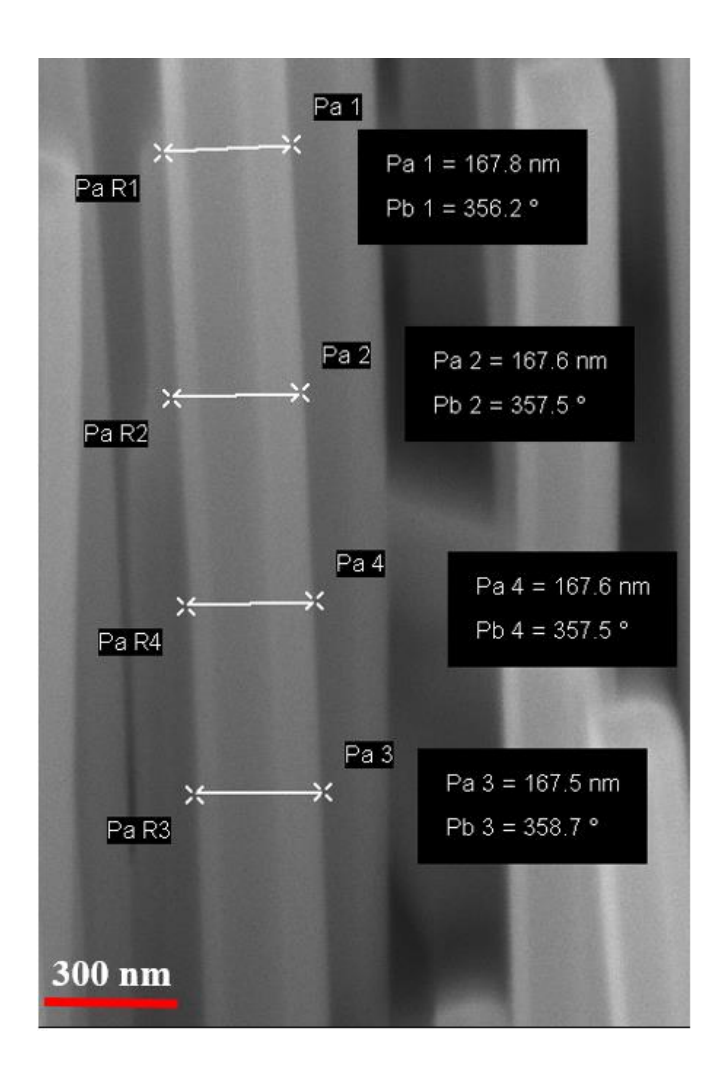


Figure S2. SEM image of Te-doped NW depicting the uniform diameter along the NW axis.

Only the tip the diameter is somewhat different due to the droplet consumption. We do not see any tapering of the NW as in B-doped GaAs NWs referred by the reviewer.

27

28

25

24

Section 3: Variation of microstructural properties with doping

(a) 50nm (b) 50nm

Figure S3. Variation of microstructural properties in (a) sample 550 and (b) sample 570

The crystallographic defect density at the NW top is higher in sample 570 than in sample 550, as shown in figure S4, which is attributed to the increased doping induced disorder at higher $T_{\text{GaTe.}}$

Section 4: SNW and ensemble NW PL emission characteristics:

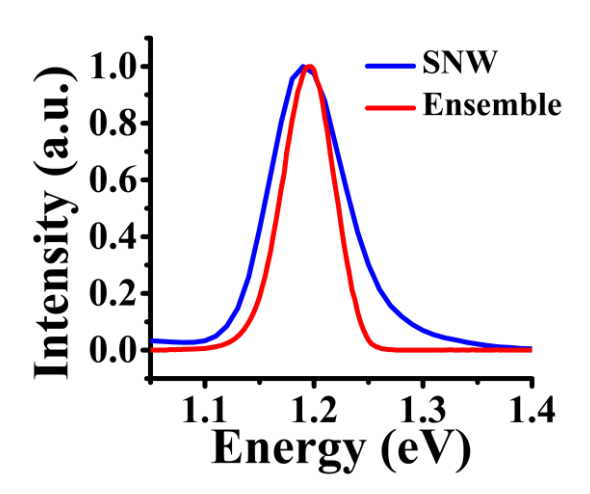


Figure S4. Comparison of PL emission from the SNW and ensemble 550 NWs.

Configuration	Energy (eV)	FWHM (eV)
Single nanowire (SNW)	1.19	0.08
Ensemble	1.19	0.06

The discrepancy in the PL line width of SNW and ensemble NWs is attributed in part to the difference in the quality of NWs near the tip and mid segment of the NW, as PL probes different segment of the NWs, the mid segment in horizontal SNW as opposed to the tip in vertical ensemble NWs. Also, variation amongst the NWs contributing to the observed variation cannot be ruled out.

Section 5: Schemetic of ensemble NW photodetector

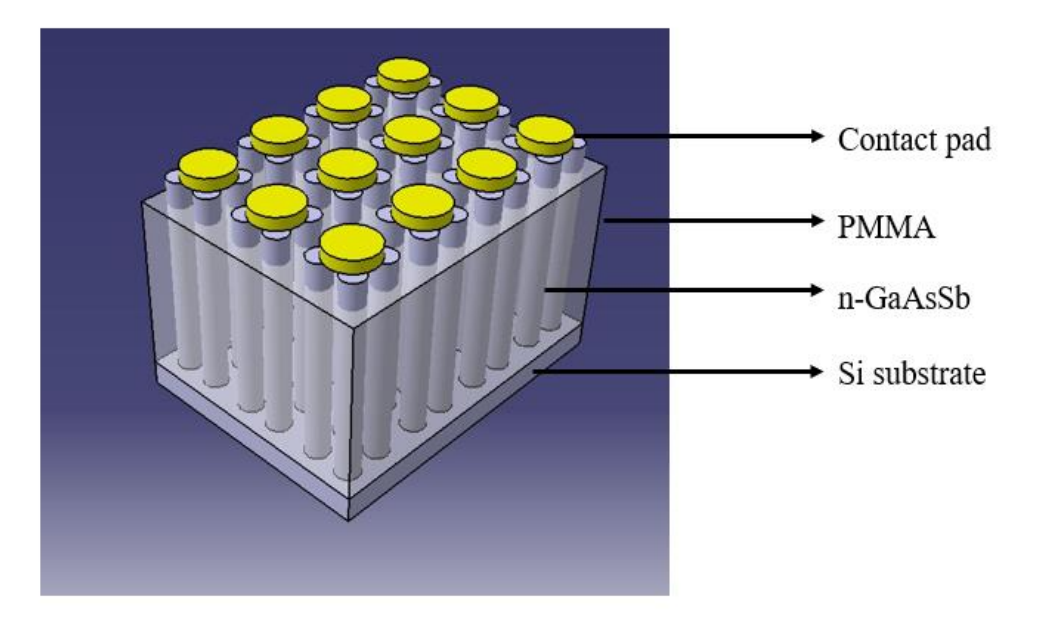


Figure S5. Schematic of ensemble NW photodetector

Section 6: SNW and ensemble NW dark I-V characteristics

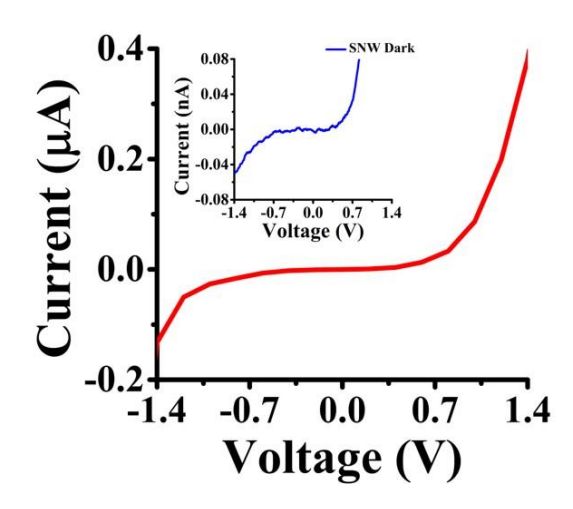


Figure S6. Comparison of SNW and ensemble I-V characteristics

Observation of similar dark I-V characteristics in both SNW (inset) and ensemble configuration in sample 550 from figure S6 suggests the compositional homogeneity in the Te-doped NWs.